Available online at www.sciencedirect.com

ScienceDirect

Ceramics International 37 (2011) 913–920

CERAMICS INTERNATIONAL

www.elsevier.com/locate/ceramint

Powder morphology modification and sinterability improvement of $Ce_{0.8}Sm_{0.2}O_{1.9}$ derived from solution combustion process

Qing Xu [a,*], Duan-Ping Huang [a], Kai Zhao [a], Wen Chen [a], Min Chen [b,1], Bok-Hee Kim [b]

[a] School of Materials Science and Engineering, Wuhan University of Technology, Wuhan 430070, China
[b] Department of Hydrogen and Fuel Cells Engineering, Hydrogen & Fuel Cell Research Center, Chonbuk National University, Jeonju 561756, Republic of Korea

Received 1 July 2010; received in revised form 23 July 2010; accepted 29 October 2010
Available online 9 December 2010

Abstract

$Ce_{0.8}Sm_{0.2}O_{1.9}$ powders were synthesized by solution combustion process using a relatively low fuel (urea) concentration. The morphology of the powders was studied in relation to the synthetic process. The sinterability and microstructure of the ceramic specimens were investigated with respect to the powder morphology. The as-combusted powder showed sphere-like fine particles constituted by an aggregation of $Ce_{0.8}Sm_{0.2}O_{1.9}$ nanocrystallites. A ball-milling process modified the morphology of the powder and improved the sinterability of the ceramic specimens. The fuel concentration of the combustion synthetic system played an important role in determining the morphology and the sintering reactivity of the resulting powders. The microstructure evolution of the ceramic specimens with sintering temperature was found to be closely related with the powder morphology. $Ce_{0.8}Sm_{0.2}O_{1.9}$ ceramics with high relative densities (95.8–98.0%) and fine grains (0.2–0.3 μm) were prepared from the ball-milled powder at relatively low sintering temperatures of 1100–1200 °C.

Keywords: A. Milling; A. Powder: chemical preparation; A. Sintering; B. Microstructure-final

1. Introduction

Doped-ceria solid solutions have drawn increasing interest as promising electrolytes for intermediate temperature (600–800 °C) solid oxide fuel cells (IT-SOFCs) due to their high oxygen-ion conductivity. The oxygen-ion conductivities of ceria-based electrolytes doped with various aliovalent cations, such as Ca^{2+}, Y^{3+}, La^{3+}, Gd^{3+} and Sm^{3+}, have been extensively evaluated in view of the IT-SOFC application [1–3]. Among them, samarium-doped ceria electrolytes have been found to exhibit superior conductivity at fixed doping levels [2].

As well-known, the solid electrolytes of SOFCs should be highly dense to meet the gas-tight requirement. Anode-supported configurations have currently been recognized as the mainstream of IT-SOFC designs as they allow for reducing the thickness of electrolyte layers and ohmic loss of the cells [4,5]. Co-sintering an electrolyte together with an anode-support has been a widely employed technology to fabricate IT-SOFC devices. Correspondingly, it is required to densify the electrolytes at relatively low temperatures (e.g. <1300 °C) to ensure satisfactory open porosity and consequently high electrocatalytic reactivity for the anodes [6,7]. Unfortunately, low-temperature sintering of doped-ceria electrolytes is difficult due to a refractory nature of ceria and a retarding effect of dopants on densification [8]. Doped-ceria electrolytes prepared by the conventional solid-state method necessitate quite high sintering temperatures of 1600–1800 °C to obtain the desired density [9,10]. There are currently two approaches to improve the sinterability of doped-ceria electrolytes. One is adopting nanocrystalline doped-ceria powders synthesized by various wet-chemical methods, such as sol–gel [11], oxalate coprecipitation [12,13], hydrothermal synthesis [14] and glycine–nitrate process [15]. The powders derived from these methods showed improved sintering reactivity, but still required relatively high sintering temperatures of 1400–1500 °C to attain reasonable densification. Another is adding transition metal oxides (e.g. cobalt oxide) as sintering aids, which has been found to be extremely effective in promoting the sintering

---

[*] Corresponding author. Tel.: +86 27 87863277; fax: +86 27 87864580.
E-mail address: xuqing@whut.edu.cn (Q. Xu).

[1] Present address: Department of Chemical and Materials Engineering, University of Alberta, Edmonton T6G 2R3, AB, Canada.

0272-8842/$36.00 © 2010 Elsevier Ltd and Techna Group S.r.l. All rights reserved.
doi:10.1016/j.ceramint.2010.10.036

of nano-sized doped-ceria powders via a transient liquid phase sintering mechanism [16,17]. Nevertheless, the addition of the oxides resulted in a remarkable deterioration of grain-boundary conduction and thus a degradation of the total conductivity [6,16]. Recently, doped-ceria powders synthesized by carbonate coprecipitation method have been confirmed to be highly reactive, enabling the densification of the powders at sintering temperatures as low as 1000–1250 °C [18–22]. This method, however, suffers from somewhat complicated procedures. Therefore, developing facile methods to prepare highly reactive doped-ceria powders appears as an intriguing subject with practical importance.

Combustion synthesis has gained reputations as a simple and speedy route to produce fine complex-oxide powders [23]. Doped-ceria electrolytes have been prepared by combustion synthesis utilizing various fuels [15,24,25]. Solution combustion process using urea as fuel has been reported to be a suitable route to prepare uniform nanometric doped-ceria powders [26]. We have prepared $Ce_{0.8}Sm_{0.2}O_{1.9}$ powder using the urea-combustion method in previous work [27]. With the aid of a ball-milling process, the powder was sintered to a relative density of over 95% at 1250 °C. Despite these progresses, a further research on the urea-combustion synthesis of doped-ceria electrolytes is necessary from the viewpoint of the co-sintering technology. Unlike the preparation of ceramics, the fabrication of electrolyte layers on anode-supports usually does not involve a high-pressure process [28]. Thus, further improving the sinterability of doped-ceria electrolytes synthesized by the urea-combustion method would leave a larger space for controlling the co-sintering of the two components and modifying the microstructure of the resulting cells. On the other hand, the morphology of doped-ceria powders prepared by the urea-combustion method has not been fully understood. Meanwhile, there has been little research on the effect of the powder morphology on the sinterability and microstructure of the ceramics. A deep insight into these issues would, in turn, lead to a clue to optimizing the preparation of doped-ceria electrolytes.

In this work, we prepared $Ce_{0.8}Sm_{0.2}O_{1.9}$ powders by urea-combustion method using a lower fuel concentration compared with our earlier work [27]. The morphology of the resulting powders was examined in view of the preparation process. The sinterability and microstructure of the ceramic specimens were investigated with respect to the powder morphology.

2. Experimental

Reagent grade $Ce(NO_3)_3{\cdot}6H_2O$, $Sm(NO_3)_3{\cdot}6H_2O$ and $CO(NH_2)_2$ (urea) were used as starting materials for synthesizing $Ce_{0.8}Sm_{0.2}O_{1.9}$ powder. The nitrates and urea were dissolved into deionized water in a beaker, followed by stirring to form a transparent aqueous solution. The mole ratio of urea to the total metal cation content (abbreviated as U/M^{n+} hereafter) was 2.0. The precursor solution was heated on a hot plate until auto-ignition combustion occurred. The as-combusted powder was milled for 48 h in ethanol medium with zirconia balls in a polyethylene jar. The powder preparation procedures are basically identical to our prior work except a larger U/M^{n+} (3.0) of the previous research [27]. The as-combusted and ball-milled powders were uniaxially pressed into discs (13 mm in diameter and 1.5 mm in thickness) and rectangular bars (32 mm × 6 mm × 6 mm). The disks were sintered at 1050–1450 °C for 4 h in air.

The phase purity of the powders and crystal structure of the ceramic specimens were investigated by a Philips X'pert PBO X-ray diffractometer using Cu Kα radiation. The average crystallite size of the powders was calculated from measured X-ray diffraction (XRD) data according to the Scherrer formula using the Jade 5.0 software. The thermogravimetry (TG) and differential scanning calorimetry (DSC) analyses of the as-combusted powder were conducted using a Netzsch STA 449C simultaneous thermal analyzer at a heating rate of 10 °C/min in air. The morphology of the powders was investigated by a JMS-5610LV scanning electron microscope (SEM), a S-4700 field emission scanning electron microscope (FESEM) and a JEM-2100F field emission transmission electron microscope (FETEM), respectively. The Brunauer–Emmett–Teller (BET) analysis of the powders was performed at a Micromeritcs Gemini 2380 surface area analyzer using liquid nitrogen adsorbent.

The dilatometric measurement was carried out at a Netzsch DIL 402C dilatometer using the rectangular bars at a heating rate of 10 °C/min between 30 and 1450 °C in air. The microstructure of the ceramic specimens was investigated at the FESEM apparatus using polished and thermally etched surfaces. The grain size of the specimens was estimated from image analysis using the Image-Pro Plus 6.0 software. The bulk densities of the specimens were measured by the Archimedes method with ethyl alcohol as the medium. The relative densities of the specimens were calculated from the measured results and the theoretical densities calculated based on measured XRD data using the Jade Software.

3. Results and discussion

3.1. Characterization of powder morphology

Fig. 1 shows the XRD pattern of the as-combusted powder. For comparison purposes, the XRD pattern of the powder

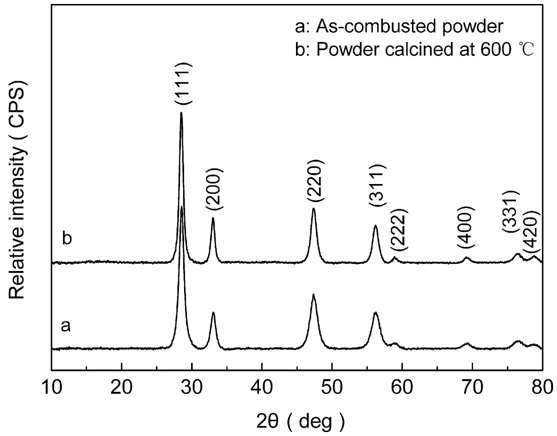

Fig. 1. XRD patterns of the as-combusted powder and the powder calcined at 600 °C for 1 h.

calcined at 600 °C for 1 h is also shown in Fig. 1. The XRD patterns of the two powders are basically identical except moderately varied peak intensities, which could be readily indexed to the cubic fluorite structure of $Ce_{0.8}Sm_{0.2}O_{1.9}$ (JCPDS Card No. 75-0158). The average crystallite sizes of the as-combusted and calcined powders were calculated to be 6.5 and 9.3 nm, respectively. The results identify a direct formation of nanocrystalline $Ce_{0.8}Sm_{0.2}O_{1.9}$ powder via the combustion process.

Fig. 2 shows the TG–DSC curves of the as-combusted powder. No remarkable change could be detected from the DSC curve. The TG curve showed weight losses of 3.1% and 4.7% before 200 °C and between 200 and 600 °C, respectively. The former weight loss is attributed to the loss of absorbed water, while the latter is assignable to the decomposition and burning of residual carbon components. The content of residual carbon components is comparatively larger than that (2.9%) of our previous work [27]. This phenomenon is assumed to be due to the lower U/M^{n+} (2.0) of the present work relative to that (3.0) of the previous work, which led to less intense combustion.

Fig. 3 shows the morphology of the as-combusted powder. The SEM image (Fig. 3a) offered a panoramic view of the powder morphology, showing fine particles with a mild agglomeration. The FESEM image (Fig. 3b) indicated a nearly spherical shape for the particles. Two sorts of particles distinct in size could be observed, with the large particles (100–150 nm) being formed by an agglomeration of the fine ones (about 30 nm). The low magnification FETEM image (Fig. 3c) revealed that the sphere-like particles had a spongy feature. The high magnification FETEM image (Fig. 3d) showed that the particles were constituted by an aggregation of nanometric crystallites. Fig. 3e shows the high resolution FETEM image of the particles. The inset in Fig. 3e is the fast Fourier transition (FFT) pattern. The ring configuration of the FFT pattern certified a polycrystalline nature of the particles, which is consistent with the aggregation of the nanocrystallites as shown in Fig. 3d. Discrete nanocrystallites could be found at the edge of the particles, as indicated by the ellipse circle in Fig. 3e. The size of these nanocrystallites was estimated to be about 5 nm, roughly agreeing with the average crystallite size (6.5 nm) determined from XRD analysis. These nanocrystallites displayed lattice fringes aligning along the same direction. The inter-fringe distance was determined to be 0.31 nm by using the Digital Micrograph software (Fig. 3f), complying with the distance between the (1 1 1) crystallographic planes of the cubic $Ce_{0.8}Sm_{0.2}O_{1.9}$ (0.3167 nm, JCPDS Card No. 75-0158).

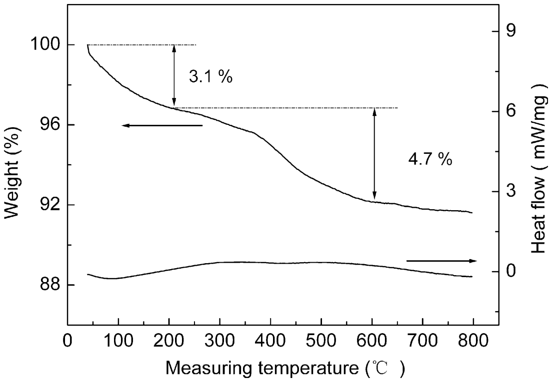

Fig. 2. TG–DSC curves of the as-combusted powder.

The average crystallite size of the ball-milled powder was calculated to be 6.7 nm from its XRD data (not shown here), essentially coinciding with that of the as-combusted powder. Fig. 4 shows the morphology of the ball-milled powder. Compared to the as-combusted powder, the ball-milled powder became finer and more uniform (Fig. 4a). The size of the particles was reduced and the shape of the particles turned to be somewhat irregular (Fig. 4b). These morphological changes are attributed to a fragmentation of the particle agglomerates in the as-combusted powder by the ball-milling. Moreover, the aggregation of the nanocrystallites appeared to be less compact after the ball-milling (Fig. 4c). A large amount of loosely aggregated nanocrystallites (about 5 nm) were discernable at the edge of the particles (Fig. 4d).

The BET analysis indicated that the as-combusted and ball-milled powders had specific surface areas of 11.6 and 34.7 m^2/g, respectively. The average particle size of the two powders was calculated according to the following equation [21]:

$$D_{BET} = \frac{6 \times 10^3}{d_{th} S_{BET}} \qquad (1)$$

where the D_{BET} is the average particle size, the S_{BET} is the BET specific surface area, and the d_{th} is the theoretical density of $Ce_{0.8}Sm_{0.2}O_{1.9}$. The two powders showed average particle sizes of 72.4 and 24.2 nm, respectively, generally according to the FESEM observation (Figs. 3b and 4b).

The morphological feature of the powders is believed to be essentially determined by the combustion synthetic process. The urea employed in the combustion synthetic process principally has dual functions, i.e., the complexant of the metal cations and the fuel of the combustion reaction. Intense combustion reaction between the fuel and oxidants generated high temperature, which is believed to be responsible for the rapid formation of $Ce_{0.8}Sm_{0.2}O_{1.9}$ [26]. Theoretically, the overall chemical reaction can be depicted by the following equation [26,27]:

$$\begin{aligned} &8Ce(NiO_3)_3 \cdot 6H_2O + 2Sm(NiO_3)_3 \cdot 6H_2O \\ &\quad + 20CO(NH_2)_2 \rightarrow 10Ce_{0.8}Sm_{0.2}O_{1.9} + 35N_2(g) \\ &\quad + 20CO_2(g) + 100H_2O(g) + 5.5O_2(g) \end{aligned} \qquad (2)$$

It was observed that the combustion was ignited from one point and then propagated in swift ripples around the beaker wall, which lasted for less than 30 s. The transient high temperature is dynamically unfavorable to a full growth of the resulting $Ce_{0.8}Sm_{0.2}O_{1.9}$ crystallites, which thus produced nanometric $Ce_{0.8}Sm_{0.2}O_{1.9}$ crystallites. The nanocrystallites had large specific surface areas and high surface energies, making them highly reactive. Hence, the nanocrystallites were prone to aggregate into large particles. On the other hand, the release of a large quantity of the gases resulting from the

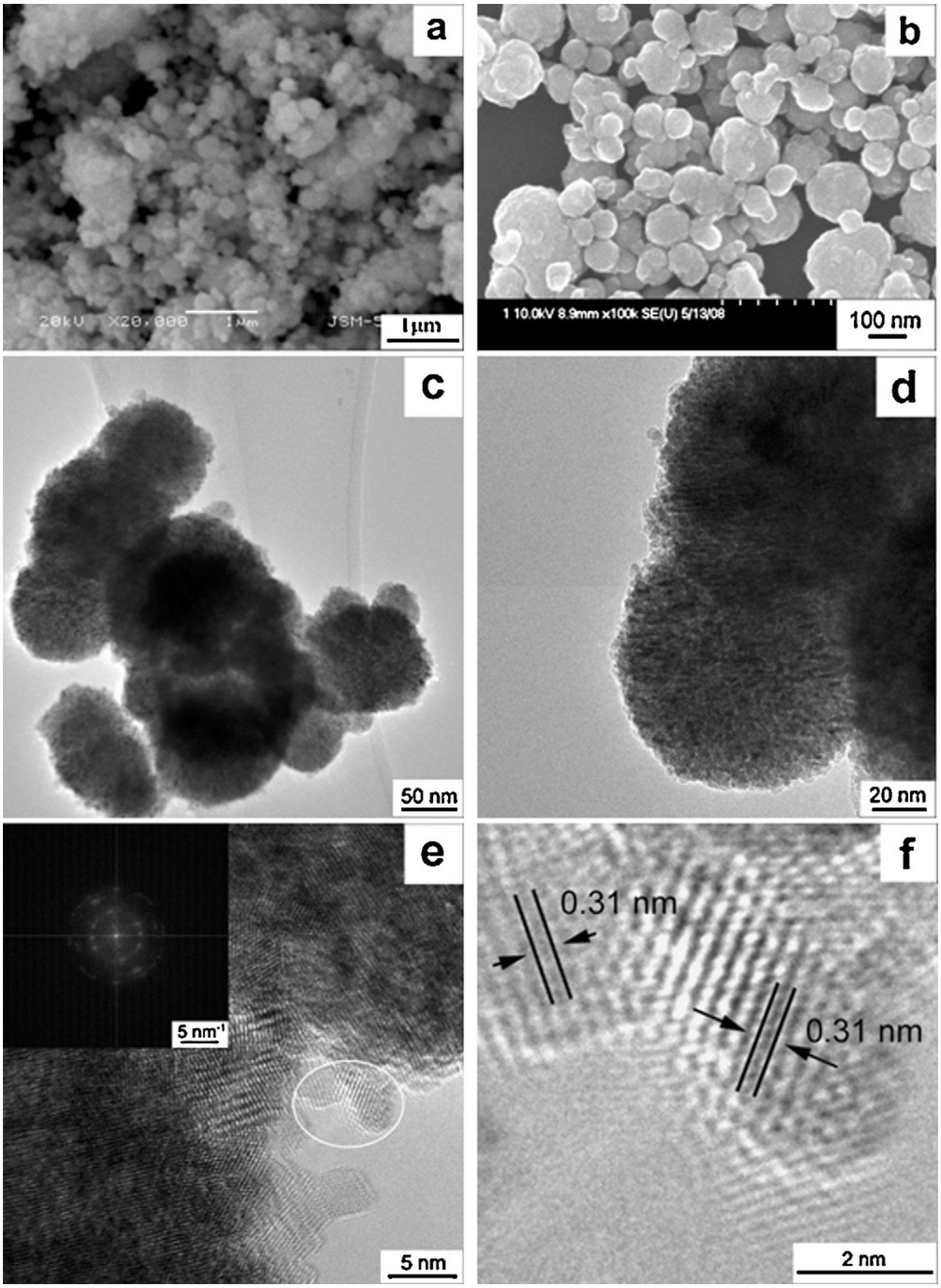

Fig. 3. Morphology of the as-combusted powder: (a) SEM image, (b) FESEM image, (c) low magnification FETEM image, (d) high magnification FETEM image, (e) high resolution FETEM image and (f) illustration of the determination of inter-fringe distance. The inset in the part (e) is the FFT pattern. The part (f) is selected from the part (e) as indicated by the ellipse circle.

combustion reaction served to prevent the formation of large aggregates of the nanocrystallite and hard agglomeration of the particles. The combination of these effects led to fine particles with a soft agglomeration. The nearly spherical particle shape is assignable to a thermodynamic reason, with the shape being favorable for the particles to achieve low specific surface energies.

The ball-milling of the as-combusted powder mainly caused two morphological changes. One is the break-up of the particle agglomerates, leading to reduced particle size. This occurrence, in turn, certifies the soft nature of the particle agglomeration in the as-combusted powder. Another is the weakening of the aggregation of the nanocrystallites, as substantiated by the comparison of Figs. 3c and 4c.

3.2. *Sinterability and microstructure of $Ce_{0.8}Sm_{0.2}O_{1.9}$ ceramics*

Fig. 5 shows the dilatometric curves of the compressed bars prepared from the as-combusted and ball-milled powders, respectively. The two specimens presented an analogous shrinkage behavior. The shrinkage of the two specimens

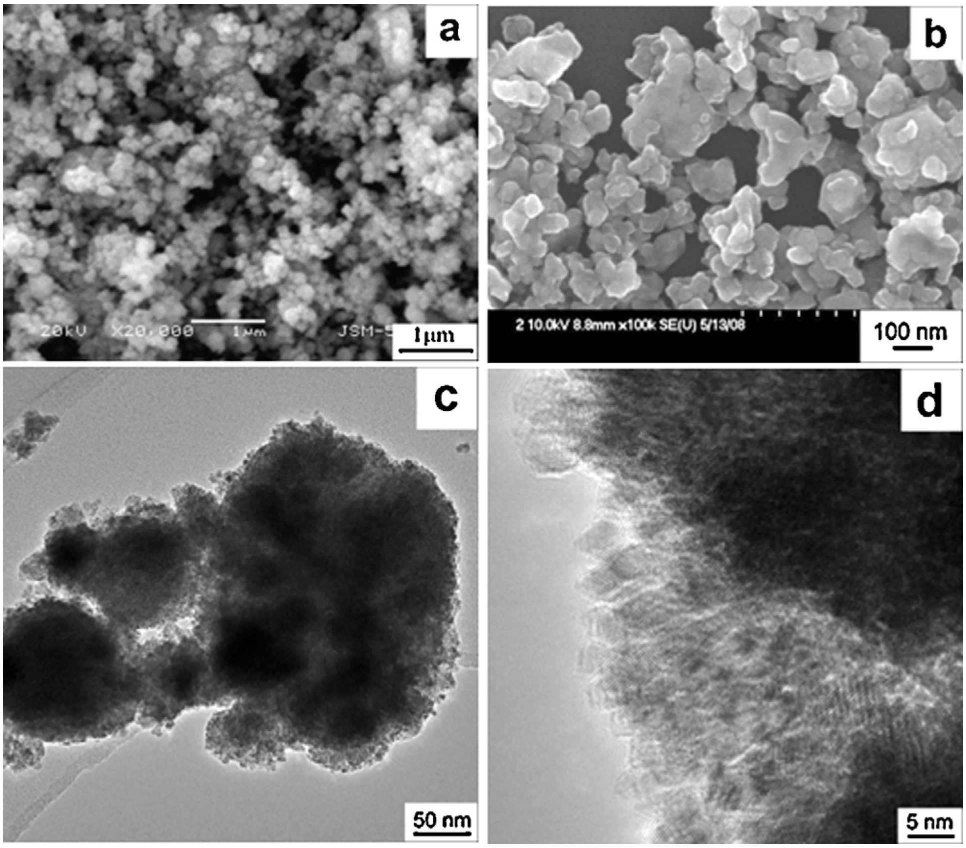

Fig. 4. Morphology of the ball-milled powder: (a) SEM image, (b) FESEM image, (c) low magnification FETEM image and (d) high resolution FETEM image.

before 600 °C can be attributed to the loss of absorbed water and elimination of residual carbon components. The as-combusted specimen reached shrinkage-rate maxima of 2.1×10^{-2} and 1.8×10^{-2}%/°C at around 750 and 1210 °C, respectively. By comparison, the ball-milled specimen displayed a facilitated shrinkage behavior, attaining shrinkage-rate maxima of 2.5×10^{-2} and 2.0×10^{-2}%/°C at around 750 and 1150 °C, respectively. The shrinkage of the two specimens tended to be saturated from 1340 and 1320 °C, showing the total shrinkage values of 14.6% and 15.9%, respectively. The dilatometric analysis infers a higher reactivity for the ball-milled powder.

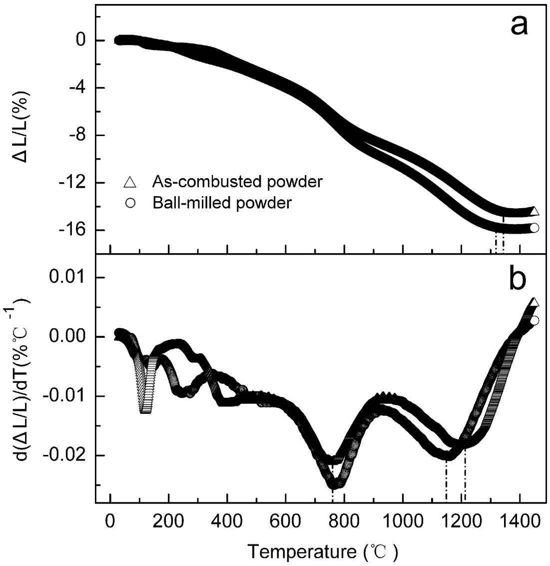

Fig. 5. Dilatometric curves of the compressed bars prepared from the as-combusted and ball-milled powders, respectively. The dashed lines indicate the temperatures of shrinkage-rate maxima and onset points of shrinkage saturation.

Fig. 6 shows the microstructure evolution with sintering temperature for the ceramic specimens prepared from the ball-milled powder. The specimen sintered at 1050 °C had a porous microstructure, showing fine grains (about 100 nm) and close contacts between two adjacent grains along the grain-boundaries. The microstructure of the specimen sintered at 1100 °C became dense without a considerable increase in grain size (about 160 nm). Sintering at the higher temperatures up to 1300 °C produced dense microstructures with steadily increased grain sizes. The specimens sintered at 1350 and at 1400 °C, respectively, showed micro-pores at the grain-boundaries. Similar phenomena have been reported for ceria-based ceramics prepared from nano-sized powders, which were assigned to the release of oxygen gas caused by redox reaction of cerium at high sintering temperatures [21,22,29].

Fig. 7 shows the relative density and average grain size as a function of sintering temperature for the ceramic specimens prepared from the ball-milled powder. The data of the specimens prepared from the as-combusted powder are also shown in Fig. 7 for comparison purposes. As can be anticipated from the dilatometric analysis, the ball-milled specimens

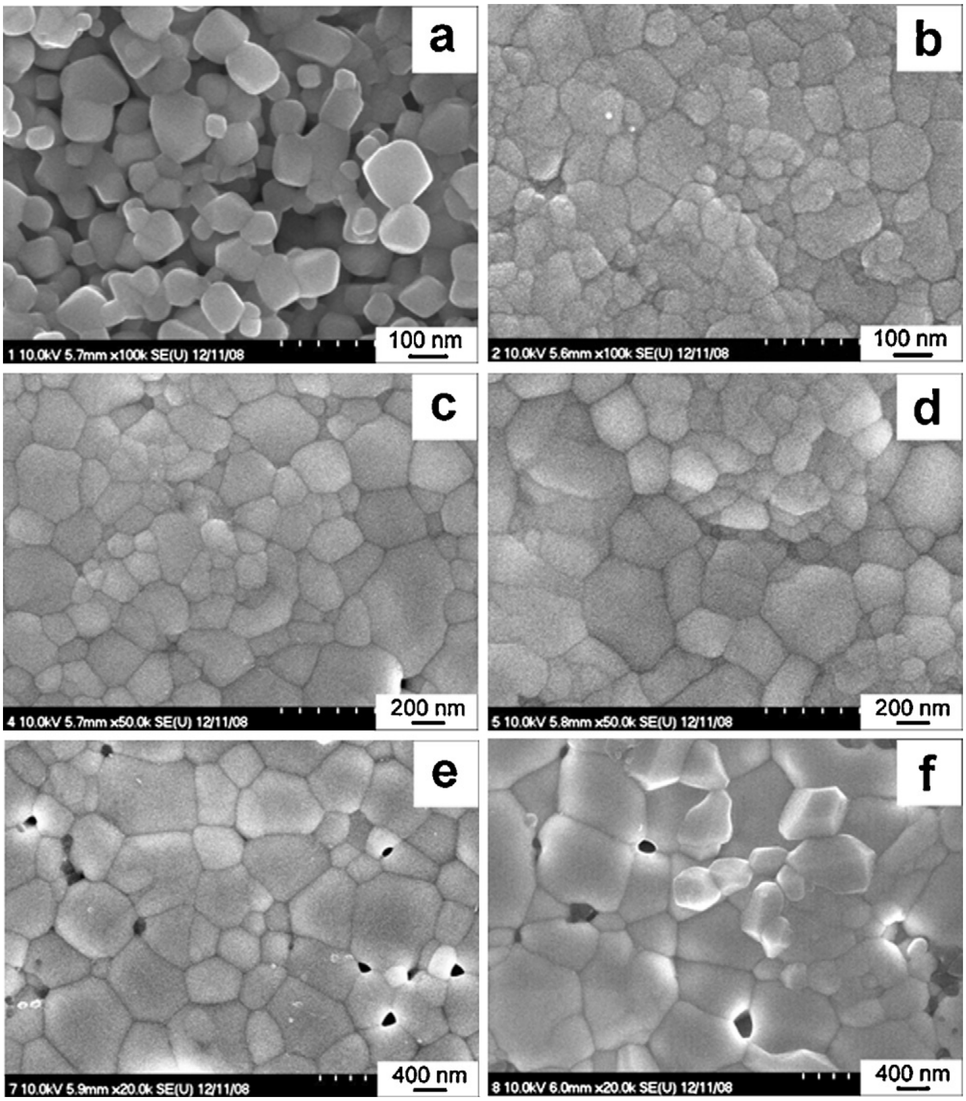

Fig. 6. FESEM images of the ceramic specimens prepared from the ball-milled powder and sintered at (a) 1050 °C, (b) 1100 °C, (c) 1200 °C, (d) 1300 °C, (e) 1350 °C and (f) 1450 °C.

exhibited a higher sinterability. The relative densities of the as-combusted specimens exceeded 95% at 1250 °C and then slightly varied at higher sintering temperatures. As for the ball-milled specimens, the relative densities sharply increased with sintering temperature from 80.1% at 1050 °C to 95.8% at 1100 °C, which is well consistent with the microstructures of the specimens sintered at the two temperatures, respectively. Afterwards, the relative densities slowly increased with sintering temperature up to a maximum value (98.0%) at 1200 °C and then tended to decline. The sinterability of the ball-milled specimens is roughly comparable with the impressive results of doped-ceria specimens prepared by the carbonate coprecipitation method [18–22].

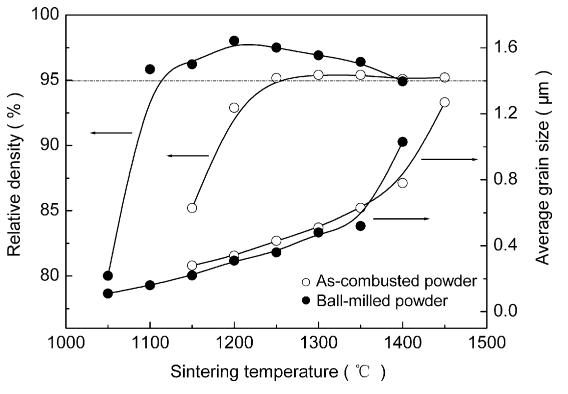

Fig. 7. Relative density and average grain size as a function of sintering temperature for the ceramic specimens prepared from the as-combusted and ball-milled powders, respectively.

The high sintering reactivity of the ball-milled powder can be tentatively explained in terms of its morphological feature. The first shrinkage-rate maximum at around 750 °C (Fig. 5b) characterizes early-stage sintering of the powder. The shrinkage during this stage mainly originated from two contributions. One is the removal of fine pores out from the aggregates of the nanocrystallites [30]. With the elimination of the intra-aggregate pores, the aggregated nanocrystallites progressively became compact and the nano-sized particles gradually grew into fine grains. Another came from the rearrangement of the fine grains [6,31]. Grain rearrangement has been suggested to be greatly contributive to early-stage sintering for nano-sized complex-oxide powders [6,31–33]. The rearrangement increased contact areas between the fine grains, not only contributing to the shrinkage of the early-stage sintering but also paving the way to further densification in final-stage sintering. The second shrinkage-rate maximum at around 1150 °C (Fig. 5b) corresponds to the final-stage sintering. The low onset temperature (1100 °C, Figs. 6b and 7) for the densification of the ceramic specimens implies that grain-boundary diffusion might play a determinant role in the final-stage sintering, which is much faster than bulk diffusion at low sintering temperatures [21,32,33]. In view of the discussion, one can conclude that the size of the nanocrystallites, the degree of the nanocrystallite aggregation and the size of the particles are crucial to the shrinkage behavior. As has been pointed out, the ball-milling process reduced the size of the particles and weakened the aggregation of the nanocrystallites. These morphological changes benefit the proceeding of densification process. Therefore, the modification of powder morphology is believed to account for the higher sintering reactivity of the ball-milled powder compared to the as-combusted powder.

It can be noticed that the ball-milled specimens showed a decline in relative density after 1200 °C (Fig. 7). Similar behaviors have been found for ceria-based ceramics prepared from nano-sized powders [22,29]. This phenomenon can be explained with the redox reaction of cerium at high sintering temperatures, as described by the following equation in the Kröger–Vink notation:

$$2\mathrm{Ce}_{\mathrm{Ce}}^{\times} + \mathrm{O}_{\mathrm{O}}^{\times} \rightarrow 2\mathrm{Ce}_{\mathrm{Ce}}' + \mathrm{V}_{\mathrm{O}}^{\bullet\bullet} + \frac{1}{2}\mathrm{O}_2 \qquad (3)$$

The redox reaction has been reported to be significant at sintering temperatures over 1200 °C for pure ceria ceramics prepared from nano-sized ceria powder [29]. This circumstance is believed to be the case for the specimens of the present work on account of a similar material nature. The micro-pores at the grain-boundaries in the specimens sintered at 1350 and 1400 °C (Fig. 6e and f), respectively, can be visualized as a consequence of exaggerated redox reaction at the elevated sintering temperatures. Moreover, the phenomenon infers a preferential occurrence of the redox reaction at the grain-boundaries. This preference is attributable to two reasons. One is relatively lower energy for forming oxygen vacancies at the grain-boundaries compared with the case of in the grain-interiors. Another is high oxygen vacancy concentration in the grain-interiors resulting from the samarium doping, which suppressed the occurrence of the redox reaction from the viewpoint of defect chemistry. Hence, one can suggest excessive oxygen vacancies at the grain-boundaries. Accordingly, the negatively charged $\mathrm{Ce}_{\mathrm{Ce}}'$ tended to segregate to the grain-boundaries to maintain long-range charge neutrality. As a result, space charge layers were created at the grain-boundaries [3]. The space charge layers together with the micro-pores appearing at high sintering temperatures caused a drag effect on grain-boundary motion and thus densification development [21]. The drag effect is presumed to be responsible for the density decline of the ball-milled specimens sintered at temperatures above 1200 °C.

By comparison, the as-combusted specimens showed a flat variation in relative density after 1200 °C (Fig. 7), indicating an insignificant effect of the redox reaction on the densification of these specimens. This phenomenon is ascribed to the influence of powder morphology on the proceeding of the redox reaction. It has been reported that the reaction is less pronounced for ceria-based specimens prepared from the powders with large particles than those with fine particles [22,29].

In previous work, we produced nanocrystalline (about 11 nm) $\mathrm{Ce}_{0.8}\mathrm{Sm}_{0.2}\mathrm{O}_{1.9}$ powders by the urea-combustion method with a U/M^{n+} of 3.0 [27]. The particle size of the powder after ball-milling for 48 h was in the range of 100–200 nm. The ceramic specimen sintered at 1250 °C attained a relatively density above 95%. By comparison, the ceramic specimen prepared from the ball-milled powder obtained an analogous relative density (95.8%) at a considerably lower sintering temperature (1100 °C) in the present work. The obviously improved sintering reactivity of the powder in the present work can be attributed to its better morphology. Considering the almost identical procedures of powder preparation of the two works except different U/M^{n+} values, one can argue an important role of the U/M^{n+} on the morphology and sintering reactivity of the powders synthesized by the urea-combustion method. This argument can be quantitatively explained with regard to the synthetic process. The U/M^{n+} reflects the concentration of the fuel (urea) in the combustion system. On one hand, a high fuel concentration can produce a large amount of gases, as afore-mentioned, suppressing the formation of large particles and hard particle agglomeration. On the other hand, a high fuel concentration can result in intense combustion and high reaction temperature [26]. This occurrence can lead to large crystallites and particles together with a severe particle agglomeration. The morphology of the powders synthesized by the urea-combustion method appears to rely on the competition of the two converse effects. Comparing the results of our two works, the latter effect can be suggested to be predominant, with a relatively low U/M^{n+} being preferred for producing the powder with high reactivity. This suggestion may provide a clue to the preparation of highly reactive doped-ceria powders via the urea-combustion route.

4. Conclusions

$\mathrm{Ce}_{0.8}\mathrm{Sm}_{0.2}\mathrm{O}_{1.9}$ powders were prepared by urea-combustion method using a relatively low U/M^{n+} of 2.0. The as-combusted powder showed sphere-like fine particles constituted by an aggregation of $\mathrm{Ce}_{0.8}\mathrm{Sm}_{0.2}\mathrm{O}_{1.9}$ nanocrystallites. The powder morphology can be explained in relation to the synthetic process. A ball-milling process was confirmed to be effective in modifying the morphology of the powder and improving the sinterability of the ceramic specimens. The comparison of the present and our previous results suggests that a relatively low U/M^{n+} is preferred for the preparation of the powder with the desired morphology and high sintering reactivity. The microstructure evolution of the ceramic specimens with sintering temperature was found to be closely associated with the powder morphology. The ceramic specimens with high relative densities of 95.8–98.0% and fine grains (0.2–0.3 μm) were produced from the ball-milled powder at relatively low sintering temperatures of 1100–1200 °C. The results of this work may serve to be a guideline for the preparation of highly reactive doped-ceria powders by using the urea-combustion method.

Acknowledgments

This work was supported by Natural Science Foundation of China (50572079 and A3 Foresight Program-50821140308), Ministry of Education (200804971002) and Wuhan Science and Technology Bureau (200851430485). The authors are grateful to the International Collaborative Research Program of Jeonbuk National University (2009) for supporting the research.

References

[1] G.B. Balazs, R.S. Glass, AC impedance studies of rare earth oxide doped ceria, Solid State Ionics 76 (1995) 155–162.

[2] K. Eguchi, Ceramic materials containing rare earth oxides for solid oxide fuel cell, J. Alloys Compd. 250 (1997) 486–491.

[3] C. Tian, S.W. Chan, Ionic conductivities, sintering temperatures and microstructures of bulk ceramic CeO_2 doped with Y_2O_3, Solid State Ionics 134 (2000) 89–102.

[4] J.H Kim, R.H. Kim, K.S. Song, S.H. Hyun, D.R. Shin, H. Yokokawa, Fabrication and characteristics of anode-supported flat-tube solid oxide fuel cell,, J. Power Sources 122 (2003) 138–143.

[5] T. Suzuki, T. Yamaguchi, Y. Fujishiro, M. Awno, Improvement of SOFC performance using a microtubular, anode-supported SOFC, J. Electrochem. Soc. 153 (2006) A925–A928.

[6] T.S. Zhang, J. Ma, L.B. Kong, P. Hing, Y.J. Leng, S.H. Chan, J.A. Kilner, Sinterability and ionic conductivity of coprecipitated $Ce_{0.8}Gd_{0.2}O_{2-\delta}$ powders treated via a high-energy ball-milling process, J. Power Sources 124 (2003) 26–33.

[7] M. Chen, B.K. Kim, Q. Xu, O.J. Nam, J.H. Ko, Synthesis and performances of Ni–SDC cermets for IT-SOFC anode, J. Eur. Ceram. Soc. 28 (2008) 2947–2953.

[8] J. Ma, T.S. Zhang, L.B. Kong, P. Hing, S.H. Chan, $Ce_{0.8}Gd_{0.2}O_{2-\delta}$ ceramics derived from commercial submicron-sized CeO_2 and Gd_2O_3 powders for use as electrolytes in solid oxide fuel cells, J. Power Sources 132 (2004) 71–76.

[9] K. Eguchi, T. Setouguchi, T. Inoue, H. Arai, Electrical properties of ceria-based oxides and their application to solid oxide fuel cells, Solid State Ionics 52 (1992) 165–172.

[10] Z.L. Zhang, T.L. Wen, H.Y. Tu, Y.Z. Lu, AC impedance investigation of samarium-doped ceria, J. Electrochem. Soc. 148 (2001) A427–A432.

[11] W. Huang, P. Shuk, M. Greenbalt, Properties of sol–gel prepared $Ce_{1-x}Sm_xO_{2-x/2}$ solid electrolytes, Solid State Ionics 100 (1997) 23–27.

[12] K. Higashi, K. Sonoda, H. Ono, S. Sameshima, Y. Hirata, Synthesis and sintering of rare-earth-doped ceria powder by the oxalate coprecipitation method, J. Mater. Res. 14 (1999) 957–967.

[13] S.W. Zha, C.R. Xia, G.Y. Meng, Effect of Gd (Sm) doping on properties of ceria electrolyte for solid oxide fuel cells, J. Power Sources 115 (2003) 44–48.

[14] K. Yamashita, K.V. Ramanujachary, M. Greenbalt, Hydrothermal synthesis and low temperature conduction properties of substituted ceria ceramics, Solid State Ionics 81 (1995) 53–60.

[15] C.R. Xia, M.L. Liu, Microstructures, conductivities, and electrochemical properties of $Ce_{0.9}Gd_{0.1}O_2$ and GDC–Ni anodes for low-temperature SOFCs, Solid State Ionics 152–153 (2002) 423–1430.

[16] C Keinlogel, L.J. Gauckler, Sintering and properties of nanosized ceria solid solutions, Solid State Ionics 135 (2000) 567–573.

[17] C. Keinlogel, L.J. Gauckler, Sintering of nanocrystalline CeO_2 ceramics, Adv. Mater. 13 (2001) 1081–1085.

[18] J.G. Li, T. Ikegami, T. Mori, Reactive $Ce_{0.8}RE_{0.2}O_{1.9}$ (RE = La, Nd, Sm, Gd, Dy, Y, Ho, Er, and Yb) powders via carbonate coprecipitation. 1. Synthesis and characterization,, Chem. Mater. 13 (2001) 2913–2920.

[19] Y.R. Wang, T. Mori, J.G. Li, T. Ikegami, Low-temperature synthesis of praseodymium-doped ceria nanopowders, J. Am. Ceram. Soc. 85 (2002) 3105–3107.

[20] Y.R. Wang, T. Mori, J.G. Li, Y. Yajima, Low-temperature fabrication and electrical properties of 10 mol% Sm_2O_3-doped CeO_2 ceramics, Sci. Technol. Adv. Mater. 4 (2003) 229–238.

[21] J.G. Li, T. Ikegami, T. Mori, Low temperature processing of dense samarium-doped CeO_2 ceramics: sintering and grain growth behaviors, Acta Mater. 52 (2004) 2221–2228.

[22] H.B. Li, C.R. Xia, M.H. Zhu, Z.X. Zhou, G.Y. Meng, Reactive $Ce_{0.8}Sm_{0.2}O_{1.9}$ powder synthesized by carbonate coprecipitation: sintering and electrical characteristics, Acta Mater. 54 (2006) 721–727.

[23] M.T. Colomer, D.A. Fumo, J.R. Jurado, A.M. Segadaes, Non-stoichiometric $La_{(1-x)}NiO_{(3-\delta)}$ perovskites produced by combustion synthesis, J. Mater. Chem. 9 (1999) 2505–2510.

[24] T. Mahata, G. Das, P.K. Mishra, B.P. Sharma, Combustion synthesis of gadolinia doped ceria powder, J. Alloys Compd. 391 (2005) 129–135.

[25] J.J. Ma, C.R. Jiang, X.L. Zhou, G.Y. Meng, X.Q. Liu, Polyvinyl alcohol-induced low temperature synthesis of CeO_2-based powders, J. Power Sources 162 (2006) 1082–1087.

[26] E. Chinarro, J.R. Jurado, M.T. Colomer, Synthesis of ceria-based electrolyte nanometric powders by urea-combustion technique, J. Eur. Ceram. Soc. 27 (2007) 3619–3623.

[27] M. Chen, B.K. Kim, Q. Xu, B.K. Ahn, W.J. Kang, D.P. Huang, Synthesis and electrical properties of $Ce_{0.8}Sm_{0.2}O_{1.9}$ ceramics for IT-SOFC electrolytes by urea-combustion technique, Ceram. Int. 35 (2009) 1335–1343.

[28] H.B. Li, C.R. Xia, M.H. Zhu, Z.X. Zhou, X.L. Wei, G.Y. Meng, Increasing the sinterability of tape cast oxalate-derived doped ceria powder by ball milling, Ceram. Int. 33 (2007) 201–205.

[29] Y.C. Zhou, M.N. Rahaman, Effect of redox reaction on the sintering behavior of cerium oxide, Acta Mater. 45 (1997) 3635–3639.

[30] P. Duran, C. Moure, J.R. Jurado, Sintering and microstructural development of ceria–gadolinia dispersed powders, J. Mater. Sci. 29 (1994) 1940–1948.

[31] T.S. Zhang, P. Hing, H.T. Huang, J. Kilner, Early-stage sintering mechanisms of Fe-doped CeO_2, J. Mater. Sci. 37 (2002) 997–1003.

[32] Y. Dror, R.D. Levi, S. Baltianski, Y. Tsur, Identification of the early stage of sintering of nano-$BaTiO_3$: a comparative study, J. Electrochem. Soc. 153 (2006) F137–F143.

[33] R. Koferstein, L. Jager, M. Zenkner, T. Muller, H.P. Abicht, Shrinkage mechanism and phase evolution of fine-grain $BaTiO_3$ powder compacts containing 10 mol% $BaGeO_3$ prepared via a precursor route, Mater. Chem. Phys. 112 (2008) 531–535.